A Multiyear Ensemble Simulation of the U.S. Climate with a Stretched-Grid GCM

MICHAEL S. FOX-RABINOVITZ

Earth System Sciences Interdisciplinary Center, University of Maryland, College Park, College Park, Maryland

ERNESTO HUGO BERBERY

Department of Atmospheric and Ocean Sciences, and Earth System Sciences Interdisciplinary Center, University of Maryland, College Park, College Park, Maryland

LAWRENCE L. TAKACS AND RAVI C. GOVINDARAJU

Science Applications International Corporation, Beltsville, and Global Modeling and Assimilation Office, NASA Goddard Space Flight Center, Greenbelt, Maryland

(Manuscript received 17 August 2004, in final form 20 December 2004)

ABSTRACT

Multiyear (1987–97) limited ensemble integrations using a stretched-grid GCM, previously developed and experimented with by the authors, are employed for U.S. regional climate simulations. The ensemble members (six in total) are produced at two different regional resolutions: three members with 60-km and the other three members with 10-km regional resolution. The use of these two finer and coarser regional resolution ensemble members allows one to examine the impact of resolution on the overall quality of the simulated regional fields. For the multiyear ensemble simulations, an efficient regional downscaling to realistic mesoscales has been obtained. The ensemble means of the midtroposphere prognostic variables (height and meridional wind) show an overall good resemblance to the global reanalysis, especially for summer. Low-level features like the warm season Great Plains low-level jet are well represented in the simulations. During winter the 100-km simulations develop a southward wind east of the Rockies that is present neither in the reanalyses nor in the 60-km simulations. The analysis of the annual mean precipitation and its variance reveals that the ensemble simulations reproduce many of the observed features of a high-resolution rain gauge dataset analyzed on a $0.5° \times 0.5°$ grid. Signal-to-noise ratios are larger than 1.5 s over a major part of the United States, especially over the Midwest and also over the mountainous regions like the Rockies and the Appalachians, suggesting that the orographic forcing is contributing to a larger signal. The ratios are smaller toward the eastern and western U.S. coastlines. This result could be attributed, at least in part, to limits in the representation of the land–sea contrasts.

For comparison purposes, an additional simulation has been performed using a global uniform $2° \times 2.5°$ grid with the same number of global grid points as those of the above stretched grids. The stretched-grid GCM ensemble means show, overall, a better regional depiction of features than those of the uniform-grid GCM.

The results of the study show that even using limited ensemble integrations with a state-of-the-art stretched-grid GCM is beneficial for reducing the uncertainty of the multiyear regional climate simulation, especially when using finer 60-km regional resolution.

1. Introduction

Ensembles of forecasts or simulations reduce the uncertainties inherent in numerical models and provide additional information that is not available in a single simulation. Ensembles have become a useful tool for climate simulation and prediction.

Typical GCMs have usually a uniform resolution that is coarser than needed for a careful analysis at mesoscales of the regional climate variability and predictability. However, variable-resolution stretched-grid (SG) GCMs, developed and matured since the early 1990s are an efficient alternative to the widely and successfully used nested-grid approach, for both short-term regional forecasting and regional climate modeling.

Corresponding author address: Dr. Michael S. Fox-Rabinovitz, Room 2207, 224 CSS Bldg., ESSIC, University of Maryland, College Park, College Park, MD 20742.
E-mail: foxrab@essic.umd.edu

Stretched-grid regional climate simulations are becoming more frequent, beginning with the studies by Deque and Piedelievre (1995), Fox-Rabinovitz et al. (1997), and McGregor (1997), and continuing with the studies on regional climate change and anomalous climate events for different continents (see, e.g., Deque et al. 1998; Fox-Rabinovitz et al. 2001, 2002; McGregor and Dix 2001).

The resolution used in a uniform-grid GCM can at least be doubled over the area(s) of interest using the SG approach with redistribution of the same amount of global grid points as might be used with a uniform grid. SG-GCMs provide efficient regional downscaling to the scales necessary for the analysis of regional mesoscale features. Depending on the particular regional resolution used, the computational time can be one order of magnitude less than that for the corresponding GCM run with fine uniform global resolution that is equivalent to that of the area of interest. Moreover, the computational efficiency provided by the SG approach is not the only rationale for its practical implementation. In our view, it is equally or even more important that the following desirable properties are obtained: an efficient downscaling, self-consistent interactions of regional and global scales due to an adequate representation of long waves when using the global integration domain, and preservation of the quality of global circulation. As a result, regional mesoscale phenomena can be successfully simulated consistently with those of larger scales.

Given the promising results for climate studies resulting from individual runs of the Goddard Earth Observing System (GEOS) SG-GCM (Fox-Rabinovitz et al. 2001, 2002; Berbery and Fox-Rabinovitz 2003), this study explores the model's potential for multiyear (1987–97) regional climate simulations in a limited ensemble integration mode. In this context, the efficiency of downscaling to realistic mesoscales and the uncertainty of the simulations are investigated. This article is organized as follows: Section 2 presents the stretched-grid design and describes the model and the experimental setup. The results of the 11-yr ensemble integrations for prognostic and precipitation fields are discussed in sections 3 and 4, respectively. Section 4 also presents an analysis of the variance of the ensemble simulations and its implications for predictability. Finally, conclusions are given in section 5.

2. A brief description of the model and experimental design

a. GEOS GCM

The uniform-grid (UG) GEOS GCM was developed at Data Assimilation Office (DAO) of the National Aeronautics and Space Administration's (NASA) Goddard Space Flight Center (GSFC). The momentum equations used in the GEOS GCM are written in the "vector invariant" form, as in Sadourny (1975) and Arakawa and Lamb (1981), to facilitate the derivation of the energy and potential enstrophy conserving fourth-order differencing scheme. The thermodynamic (potential temperature) and moisture (specific humidity) equations are written in a flux form to facilitate potential temperature and moisture conservation. The Arakawa C grid is used for the horizontal approximation. For the vertical approximation an unstaggered Lorenz (1960) grid in generalized sigma coordinates is used. The vertical differencing scheme is described in Arakawa and Suarez (1983). The time integration is done with an explicit scheme based on the leapfrog method with a time-averaged pressure gradient (Schuman 1971; Brown and Campana 1978; Fox-Rabinovitz 1974). The scheme allows using time steps that are approximately twice as large as those of the leapfrog method. A complete description of the fourth-order finite-difference scheme used in the dynamical core can be found in Suarez and Takacs (1995).

The relaxed Arakawa–Schubert (RAS) cumulus convective parameterization and the re-evaporation of falling rain are based upon the works of Moorthi and Suarez (1992) and Sud and Molod (1988). The longwave and shortwave radiation are parameterized following Chou and Suarez (1994). The planetary boundary layer and the upper-level turbulence parameterizations are based on the level 2.5 closure model of Helfand and Labraga (1988) and Helfand et al. (1991). The orographic gravity wave drag parameterization follows Zhou et al. (1996).

Since the early 1990s, the GEOS GCM was routinely run with $2^\circ \times 2.5^\circ$ horizontal resolution and 70 layers in the vertical covering the entire tropospheric and stratospheric domain between the surface and the 0.01-hPa level. The GEOS GCM was used by Chang et al. (2000) and Schubert et al. (2001) for ensemble integrations for deterministic seasonal prediction. Chang et al. (2000) and Schubert et al. (2001) found that the GEOS-2 GCM internal variability and predictability are comparable to five other GCMs considered by Shukla et al. (2000).

b. The stretched-grid design

The stretched-grid design shown in Fig. 1 has a uniform (latitude $\times$ longitude) fine resolution over an area of interest that has to be a spherical rectangle. The SG design is portable so that the area of interest can be allocated over any part of the globe such as the rectangle over the United States used in this study. Outside

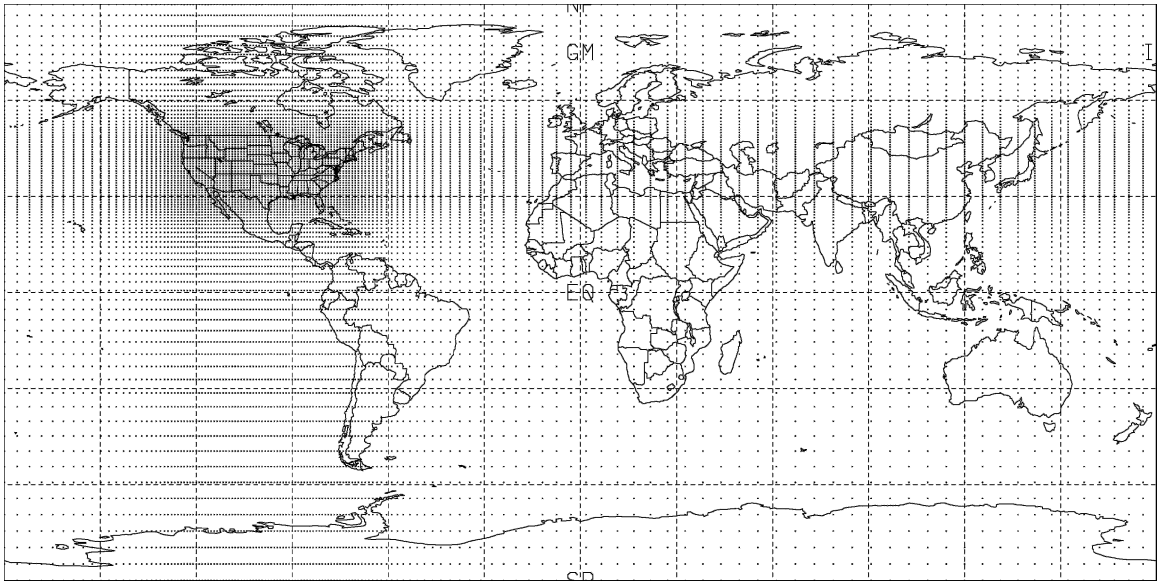

FIG. 1. A global stretched grid with area of interest over the United States.

this area, the grid intervals increase in both latitudinal and longitudinal directions as a geometric progression with a constant local stretching factor, or the ratio defined as $R_j = DX_j/DX_{j-1}$, where DX_j and DX_{j-1} are adjacent grid intervals, and j is the horizontal index. The global accuracy of the approximation is controlled by the maximal grid interval on the sphere (in both latitudinal and longitudinal directions), $DX_{max} = \max(DX_j)$.

To control undesired computational problems due to grid irregularity, the following conditions have to be imposed on the SG design (Vichnevetsky 1987; Fox-Rabinovitz 1988; Fox-Rabinovitz et al. 1997). First, the stretching should be uniform; that is, R_j should be constant for all j's outside the area of interest (within which resolution is uniform, and therefore $R_j = 1$). Second, the stretching has to be moderate in the sense that the local stretching factors do not deviate from unity by more than about 10%. This allows having fine mesoscale resolution over the area of interest (e.g., Cote et al. 1993, 1998; Cote 1997) where a significant percentage of the total number of global grid points is allocated within the area of interest, while reducing the amount of computations needed over the rest of the globe. Third, to keep the overall accuracy of the approximation under control for long-term integrations, and to be quite close to the resolution of typical GCMs, the maximal grid intervals have to be not larger than 4°–5°. In this way, a reasonable quality of the global simulated fields is obtained, thus providing consistent interactions between global and regional scales throughout the SG-GCM integrations. Fourth, fine regional resolution over the area of interest has to be uniform for a homogeneous representation of orography, land–sea differences, and other boundary forcing.

The stretched grid used in this study has the same number of grid points as a global uniform 2° × 2.5° grid but redistributed according to the SG design (Fig. 1). The area of interest has the following coordinates: 23° to 50°N and 125° to 72°W.

c. Configuration of the GEOS SG-GCM

Development of the GEOS SG-GCM for regional applications began in the early to mid-1990s at the DAO at NASA GSFC in collaboration with the University of Maryland. The variable-resolution stretched-grid version of the model (SG-GCM) has a dynamical core solved on the stretched grid with realistic orography as described by Fox-Rabinovitz et al. (1997, 2000). The numerical scheme of the GEOS GCM, with all its properties, remains unchanged when using stretched grids. Two basic horizontal filtering techniques, a refined polar or high-latitude Fourier filter (Takacs et al. 1999) and a Shapiro (1970) filter, have been adjusted to variable resolution, so that they can be applied directly to the stretched-grid fields. The orographic forcing is represented directly on the stretched grid as an integral part of the model dynamics (Fox-Rabinovitz et al. 2000). As a result, the fine regional resolution orographic forcing and its gradients make a significant impact and can lead to improvements in regional mesoscale climate simulation.

The diabatic tendencies are computed on an intermediate uniform grid and updated at the appropriate

physical/computational time scales. Then, they are interpolated, prorated per time step and applied at every time step to the model dynamics stretched grid. The resolution used for the intermediate uniform grid for calculating model physics and surface boundary forcing for this study is 2° × 2.5°. Such an approach is justified by the assumption that model physics and dynamics can be treated at different temporal and spatial resolutions (see Lander and Hoskins 1997). For a spectral model, they advocate using coarser resolution for model physics than for model dynamics, and further conclude that similar considerations also apply to finite-difference and finite-element models. Implementing model physics on an intermediate uniform resolution grid avoids some potential complications that may arise from calculating model physics parameterizations, such as convection in the Tropics on a stretched grid. Fox-Rabinovitz et al. (2001) verified that for such a combination of the SG model dynamics and intermediate uniform-grid model physics, the model physics captures the finer-scale patterns produced by the model dynamics on the stretched grid. It is worth mentioning that in addition to discussing the 1988 Midwest drought the paper also includes the discussion of precipitation and dynamic fields at other locations that have significant mesoscale structures. A further discussion on the evidence of realistic mesoscale features in prognostic and precipitation fields at the core monsoon region for the similar setup of SG-GCM is presented by Berbery and Fox-Rabinovitz (2003).

A legitimate question to ask is how much mesoscale features can be produced with the SG-GCM when using a coarser 2° × 2.5° resolution for the model physics. We acknowledge that the use of a 2° × 2.5° grid for calculating model physics is due to the significant computational resources required, even for the limited ensemble calculations (see section 2d). Nevertheless, we can still obtain meaningful details at the regional mesoscales, in a similar way as was shown in our previous papers (e.g., Berbery and Fox-Rabinovitz 2003) and in other publications on the stretched-grid approach (e.g., Deque and Piedelievre 1995; Deque et al. 1998; Cote et al. 1998; McGregor and Dix 2001). Section 4b provides evidence that, although some measurable mesoscale detail is obtained for convective precipitation, the dominant factor is the increase in mesoscale detail due to the large-scale precipitation.

Several articles have reported the performance of the GEOS SG-GCM under different conditions. Experiments with the model were part of the Project to Intercompare Regional Climate Simulations (PIRCS; e.g., Takle et al. 1999). The model was run in a special simulation mode designed to provide consistency with other participating (nested grid) models (Fox-Rabinovitz 2000). The PIRCS experiments were aimed at studying the U.S. summer anomalous climate events of the U.S. Midwest drought of 1988 and the flood of 1993. A positive impact from using a finer regional resolution (40 versus 60 km) was an additional result presented in the above paper. A diagnostic analysis of the large-scale evolution of the North American monsoon system and the mesoscale moisture surges along the Gulf of California was performed by Berbery and Fox-Rabinovitz (2003). Park et al. (2004) and Allen et al. (2004) present the results of atmospheric chemistry experiments based on the same model.

d. Experimental setup

Two model setups are employed for this study. The stretched grid is either 60 or 100 km of regional resolution, having 14 and 5 times fewer grid points than those of global uniform 60- and 100-km-resolution grids, respectively. The actual regional resolutions used within these two stretched grids are 0.6° × 0.6° and 1° × 1°, which are equivalent approximately to 54 km × 66 km and 90 km × 111 km, respectively (the longitudinal intervals were estimated at 36°N, a middle latitude of the region). For brevity, we call them 60- and 100-km regional resolutions, respectively. The local stretching factors R_j deviate from unity by less than 6% and 3.5%, and the maximal grid intervals are less than 5.5° and 4° in both latitude and longitude for the 60- and 100-km stretched grids, respectively. The total global stretching factors, or the ratios of maximal to minimal grid intervals, are approximately 9 and 4 in both the latitudinal and longitudinal directions for the 60- and 100-km stretched grids, respectively. All SG-GCM simulations have the same number of grid points, and the intermediate uniform resolution of 2° × 2.5° was used for the model physics calculations (as indicated above in section 2c).

The major positive regional impact from stretching can be directly obtained from a better-resolved model dynamics and boundary forcing, that is, orography and land–sea differences. In that sense, the improvements should be expected near small-scale terrain features and coastlines, and reflected, for example, in large-scale and total precipitation. However, some improvements associated with better-resolved land–sea differences may be obtained only when using larger ensembles.

The National Centers for Environmental Prediction (NCEP) weekly analyses of sea surface temperatures, snow, and sea ice distributions at 2° × 2° resolution and the monthly analyses of soil moisture available at 2° × 2.5° resolution are employed for surface boundary conditions. The SG-GCM experiments were started from

initial conditions in November 1986 and continued through December 1997. Initial conditions for the different ensemble members are two days apart, starting from 1 November 1986, and were obtained from analyses produced by a stretched-grid data assimilation system (GEOS SG DAS) discussed by Fox-Rabinovitz et al. (2000, 2002). Using different initial conditions results in a measurable dispersion among the ensemble members as will be shown in section 3b. The model analysis of the simulations begins at 1 January 1987 to avoid the initial spinup effects.

The 11-yr ensemble integrations include three members run with 60-km regional resolution and three other members with 100-km regional resolution, or a total of six ensemble members. All SG- GCM simulations have the same number of grid points (as indicated above in 2b).

Also, one experiment was performed with the intermediate uniform grid at $2° \times 2.5°$ grid spacing (GEOS UG-GCM), with the same number of grid points as that of the stretched grids. In the context of the further discussion, it should be noted that a single simulation is produced with UG-GCM.

The limited ensemble and UG-GCM integrations required quite significant computational resources. Each 12-yr simulation on the eight-processor Silicon Graphics, Inc. (SGI) computer took ~3.5 months, with two–three simulations run simultaneously, and ~0.9 Terabits for storing simulated prognostic and diagnostic fields for each experiment.

e. Evaluation datasets

The NCEP–National Center for Atmospheric Research (NCAR) global reanalyses (Kalnay et al. 1996) were employed to evaluate the SG-GCM prognostic fields. Precipitation simulations were compared to independent rain gauge precipitation data produced on a $0.5° \times 0.5°$ grid (land only) and available from the University of Delaware (Willmott and Matsuura 2001). The precipitation diagnostics are further complemented with the dataset called Climate Prediction Center (CPC) Merged Analysis of Precipitation (CMAP), which is discussed by Xie and Arkin (1997). These precipitation estimates are on a $2.5° \times 2.5°$ latitude–longitude grid and are the result of merging observations and several satellite products including the infrared-based Geostationary Operational Environmental Satellite (GOES) precipitation index (GPI), outgoing longwave radiation–based precipitation index (OPI), and microwave measurements. The CMAP version employed here does not include the NCEP–NCAR reanalysis precipitation.

3. Simulated prognostic fields

In this and the next section, the 11-yr (1987–97) SG-GCM ensemble simulations are assessed with a focus on the meso-to-large-scale patterns of both prognostic fields and precipitation patterns. Before discussing the regional patterns, the global features of the model simulations will be considered. It is noteworthy that the quality of global fields produced with GEOS SG-GCM was discussed in detail in previous publications by Fox-Rabinovitz et al. (2001, 2002). Here we briefly discuss it for the ensemble integrations.

Figure 2 presents the mean 500-hPa height and precipitation for 1987–97. The monthly mean heights are calculated from 6-h instantaneous data (at 0000, 0600, 1200, and 1800 UTC). Total monthly precipitation (convective plus large scale) is the mean of the 6-h accumulated data. Only SG-GCM simulation data (and no UG-GCM data) are included in the ensemble means. Although precipitation fields are discussed in detail in the next section we included a brief discussion of the simulated global precipitation and 500-hPa heights (H-500) here as an introduction to our discussion for both sections. According to Fig. 2a, which shows CMAP precipitation and 500-hPa heights for the NCEP–NCAR reanalysis, during December–January–February (DJF; boreal winter, austral summer) the areas of largest precipitation in the ensemble mean are found in the Tropics, representing the intertropical convergence zone (ITCZ), along the Northern Hemisphere Pacific and Atlantic storm tracks, and the austral summer convergence zones in the South Pacific, the South Atlantic, and southeast of Africa. All these precipitation maxima are in a close agreement with the ensemble mean precipitation (Fig. 2c). Likewise, the H-500 pattern for the NCEP–NCAR global reanalysis (Fig. 2a) bears a close resemblance to the pattern derived from the ensemble mean (Fig. 2c).

During June–July–August (JJA; boreal summer, austral winter), Fig. 2b, which presents CMAP precipitation and the NCEP–NCAR global reanalysis 500-hPa heights, shows that in addition to the ITCZ large precipitation is found associated with the monsoons in southern Asia, western Mexico, and central Africa. In the Southern Hemisphere, the precipitation pattern tends to be mostly zonal along the storm track. Again, the resemblance of ensemble means for precipitation and 500-hPa heights (Fig. 2d) to the corresponding CMAP and reanalysis fields (Fig. 2b) is noticeable.

The SG-GCM ensemble means for both seasons are capable of producing the global fields quite comparable to those of UG-GCM (Figs. 2e,f), despite using a coarser resolution far from the region of interest. Fig-

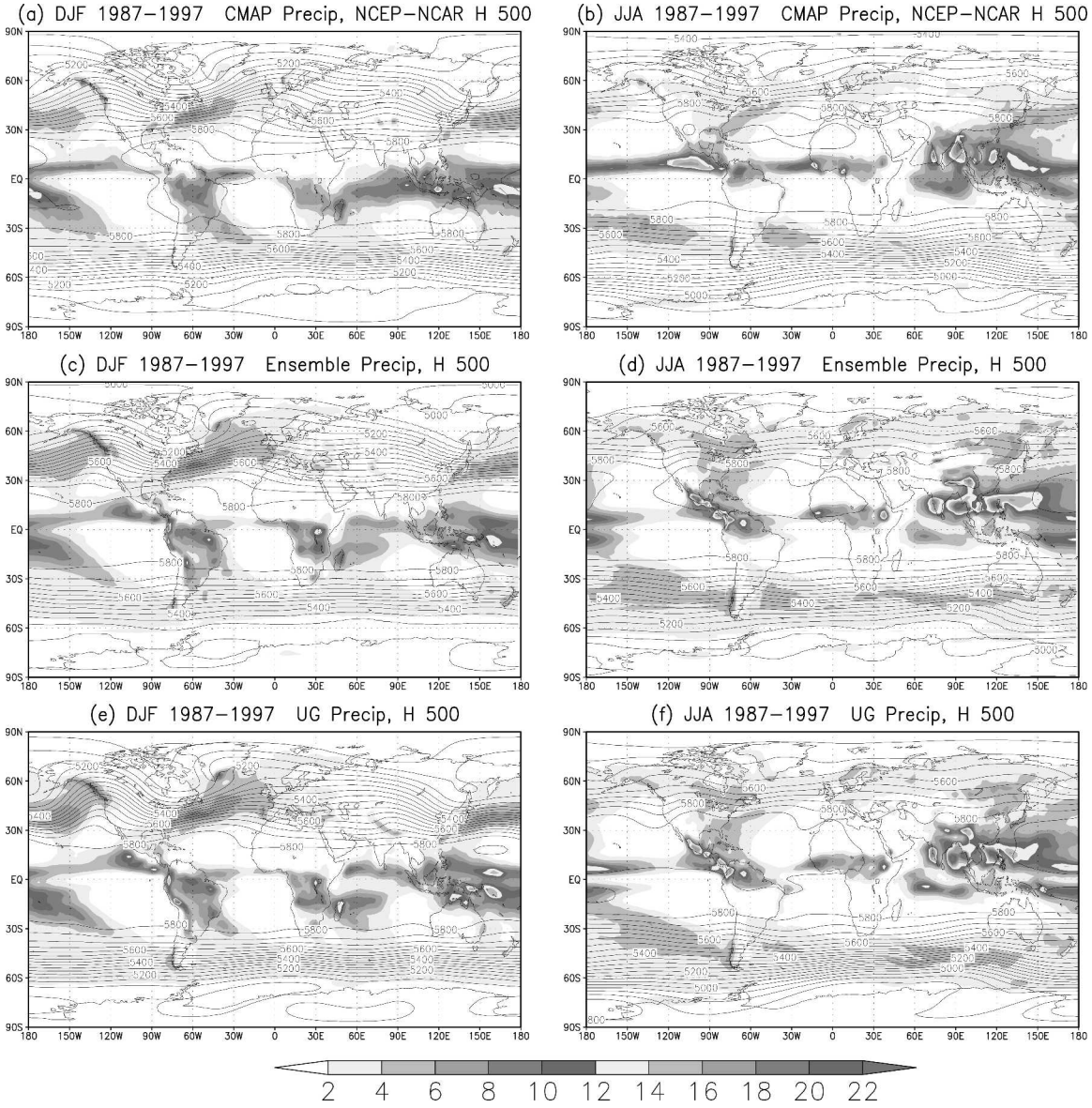

FIG. 2. The 11-yr (1987–97) mean global fields of (a) DJF 500-hPa heights and precipitation for the NCEP–NCAR global reanalysis and CMAP precipitation; (b) as in (a), but for JJA; (c) as in (a), but for the ensemble mean; (d) as in (c), but for JJA; (e) as in (a), but for UG-GCM; (f) as in (e), but for JJA. Precipitation is presented in different gray shades, and the 500-hPa heights as contours. The contour intervals for heights are 50 m, and the shading intervals for precipitation are 2 mm day^{-1}.

ure 2 (as well as other global fields that are not shown) shows global simulated fields of a sufficiently high quality, which is important for consistent interactions of global and regional scales within SG-GCM.

a. Regional simulations of ensemble mean

The 11-yr mean H-500 for winter (DJF) and summer (JJA) over the continental United States are presented for the ensemble means and the corresponding verifying NCEP–NCAR reanalyses (Fig. 3). In both seasons the ensemble patterns are similar to the verifying reanalyses. During winter, the NCEP–NCAR reanalyses (Fig. 3a) depict a western U.S. ridge and an eastern U.S. trough pattern whose positions as well as gradients are well reproduced by the ensemble mean (Fig. 3b). However, the ensemble has a regional negative bias (the difference between the ensemble and reanalyses shown by the shades) that ranges from 0 to 25 m in the southwest United States to about 75–100 m toward the northeast. During summer, both the reanalyses and ensemble mean (Figs. 3c,d) reveal a broad ridge over the central

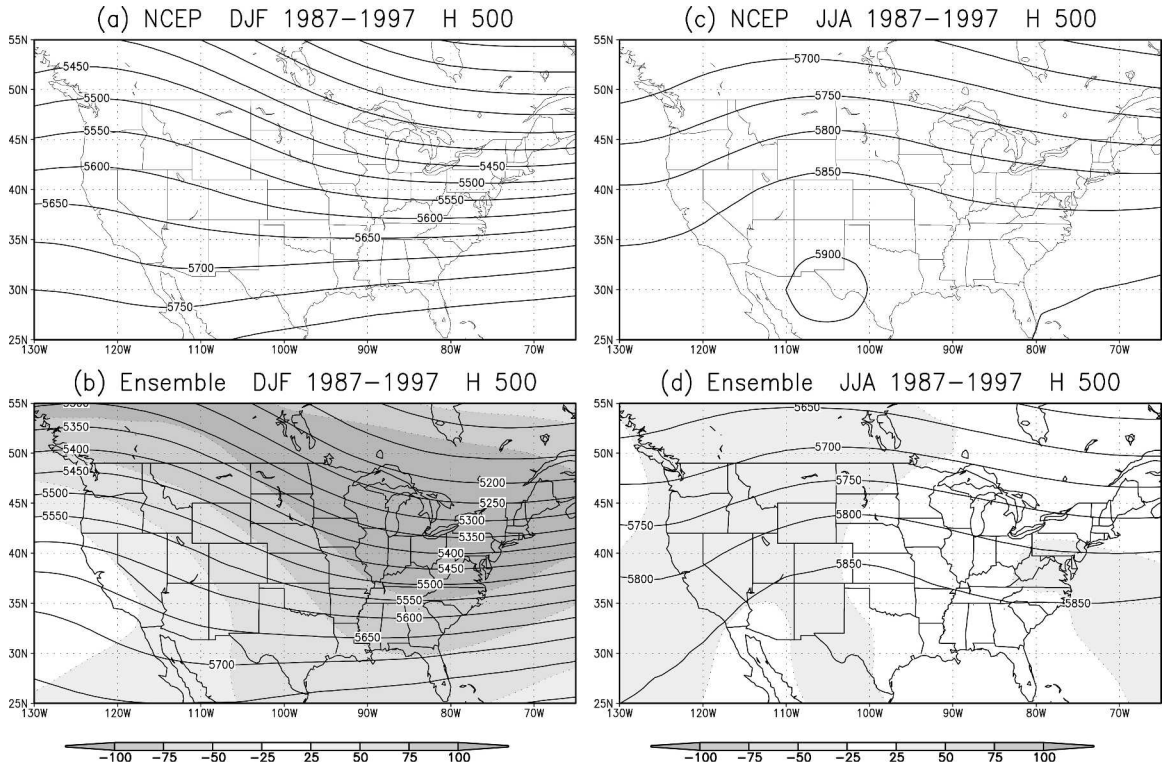

FIG. 3. The 11-yr (1987–97) mean 500-hPa heights for (a) winter (DJF) NCEP–NCAR global reanalyses, (b) winter ensemble mean and its bias, (c) summer (JJA) NCEP–NCAR global reanalyses mean, and (d) summer ensemble mean and its bias. The contour interval is 50 m. The shades in (b) and (d) represent the ensemble bias.

United States. Although the ensemble mean high pressure over northern Mexico (Fig. 3c) is slightly weaker than in the reanalyses (Fig. 3d), the negative bias is notably smaller than during winter and does not exceed 25 m in magnitude, which is close to typical observational errors.

The UG-GCM bias for H-500 (not shown) is quite close to that of the ensemble mean. Usually, 500-hPa heights are not as sensitive to resolution as the other fields, discussed below, like near the surface wind or precipitation.

The winter (DJF) and summer (JJA) meridional wind at 500 hPa (V-500) is shown in Fig. 4 for the NCEP–NCAR reanalyses, for the 60- and 100-km ensemble means and UG-GCM. During winter, both observations (Fig. 4a) and ensembles (Figs. 4b,c) have a negative maximum near the border of the United States and Canada, and a secondary maximum located over central California. The positive values spread over the southeastern United States and along the east coast and the western Atlantic Ocean. The simulated patterns are close to those of the reanalyses, but a negative 1–2 $m\,s^{-1}$ bias over the major part of the region and a positive bias over the western Atlantic Ocean are noted in the ensemble means (shades in Figs. 4b–d). A slightly larger bias is observed for the 60-km ensemble mean versus the 100-km ensemble mean in southeastern Canada in winter (Figs. 4b,c). Note, however, that the 60-km ensemble bias is considerably smaller, about 0.5–1 $m\,s^{-1}$ over almost the entire region. The UG-GCM simulation has larger bias for the V-500 annual mean (not shown) than those of the 60- and 100-km ensemble means. For the winter season, the UG-GCM simulation (Fig. 4d) has larger bias of 2–3 $m\,s^{-1}$ over the major part of the region than both the 100-, and especially, the 60-km ensemble means (Figs. 4b,c).

During summer (Figs. 4e–h), the most dominant feature in all cases is the positive maximum in the western United States and less intense and more widespread negative values in the Midwest and the eastern United States. A slightly larger bias is observed for the 60-km ensemble mean versus the 100-km ensemble mean, especially over California. For the summer season, the 100-km ensemble mean has the smallest bias over the major part of the western United States, especially over California and Nevada, but it increases over southeastern Canada and the northwestern United States, British Columbia, and the surrounding ocean (Fig. 4g). The

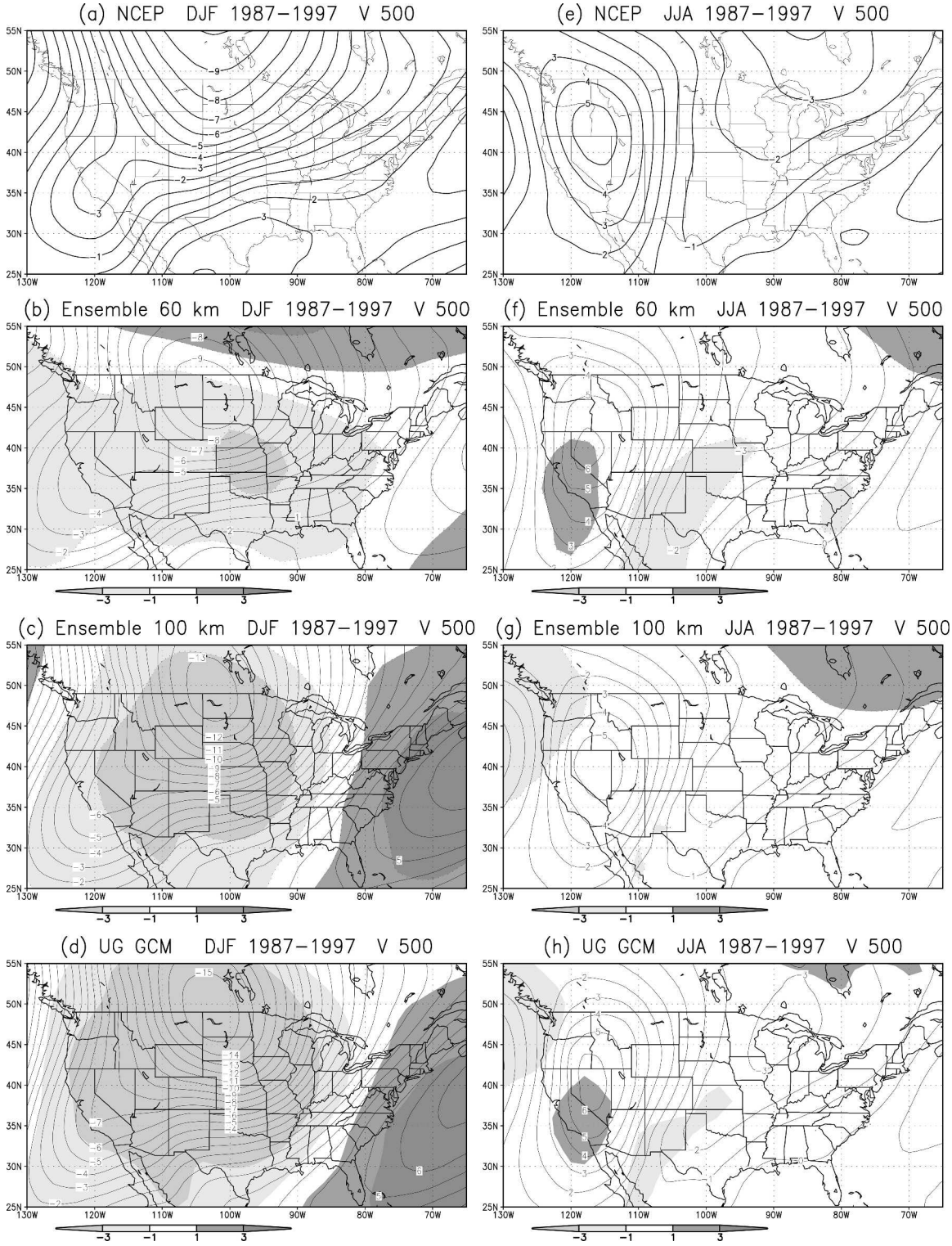

FIG. 4. The 11-yr (1987–97) 500-hPa meridional wind mean (left) DJF and (right) JJA for the (a), (e) NCEP–NCAR global reanalyses, (b), (f) the 60-km ensemble, (c), (g) the 100-km ensemble, and (d), (h) UG-GCM. The wind contour interval is 1 m s^{-1}. Shades represent the biases of the respective ensembles (contour intervals depicted below each panel).

60-km ensemble mean and UG-GCM for JJA (Figs. 4f,h) have comparable biases, with the exception of the northwestern United States, British Columbia, and the surrounding ocean where the 60-km ensemble mean has a smaller bias. As in the case of 500-hPa heights, *V*-500 biases are significantly smaller during the warm season, with the values within 0–1 m s^{-1} of either sign.

The 500-hPa level was used for Fig. 4 for consistency with other figures (Figs. 2, 3, 6, 7). Similar computations for 300- and 200-hPa levels, closer to the jet stream level, showed no significant differences in terms of the flow pattern and biases.

The low-level circulation, as depicted by the 925-hPa meridional wind is presented in Fig. 5. Probably one of the most interesting features of the circulation during summer is the presence of the Great Plains low-level jet (LLJ; Fig. 5e), which is represented, although with a slightly different shape, in the 60- and 100-km ensembles (Figs. 5f,g) and in the UG-GCM simulation (Fig. 5h). The southern part of the summer LLJ pattern (Figs. 5f–h) is slightly rotated clockwise compared to that of the reanalysis (Fig. 5e), but it still seems to originate over the Gulf of Mexico near the southeastern Texas coastline. This is suggested when analyzing the *U* and *V* components for different levels from the surface to 850 hPa (not shown).

The southward flow over the eastern Pacific is also shown in the simulations. The situation during winter is different: in the reanalyses, weak LLJ southward winds over the Great Plains (Fig. 5a) are well represented in the 60-km ensemble (Fig. 5b). On the other hand, the 100-km ensemble and UG-GCM simulations (Figs. 5c,d) tend to show much larger—and overestimated compared to the reanalyses—southward wind intensity of the order of 5–6 m s^{-1} on a narrow band, east of the Rockies. Because of the significantly overestimated DJF southward wind, the annual mean fields (not shown) of the UG-GCM and 100-km simulations do not have the signature of the LLJ that shows up in the reanalyses and 60-km ensemble.

b. Dispersion within the ensembles

While the previous analysis focused on the ensemble means, it is also important to review the spread of the simulations. Using different initial conditions for generating ensemble members results in a measurable amount of dispersion. Initial conditions a few days apart have different medium- and small-scale features. Not surprisingly, these initial differences or perturbations produce the measurable dispersion among the ensemble members shown in Figs. 6 and 7. Note that even much smaller perturbations may also produce some dispersion due to a strong nonlinearity of model physics (like convection and large-scale precipitation). Figure 6b depicts two 500-hPa contours for each simulation, 5700 and 5850 m, which are representative of the overall field during summer. It is first noticed that the pattern in the simulations is shifted south by about 4°–6° of latitude (consistent with the bias discussed earlier in Fig. 3) and, second, that the spread between members is larger toward the south. The greater spread in the southern set of contours in summer is likely because the gradient is weaker there, so that slight changes in the height field can produce relatively large displacements of a single contour. On the other hand, all members have the same ridge–trough structure. The winter situation (contours: 5500 and 5700 m) presented in Fig. 6a suggests a tighter set of curves, particularly toward the east. Again, the simulated patterns are shifted south, and the location of ridges and troughs is approximately the same, except over northwestern Mexico where the model tends to put the ridge slightly displaced to the east.

During winter (Fig. 7a) the intra-ensemble spread of the 500-hPa meridional wind contours is larger than during summer (Fig. 7b), but both are still close to the NCEP–NCAR reanalysis. It has been suggested that synoptic-scale activity tends to increase the uncertainty of the simulations during winter (see, e.g., Shukla et al. 2000). A notably closer agreement is noticed in the shape of the meridional wind during summer (Fig. 7b), particularly over the western United States. The spread of the summer simulations also appears to be smaller.

Note that the 60-km ensemble members have a larger dispersion than those of 100 km (not shown), which points to the necessity of having larger ensembles for higher-resolution ensembles.

We also calculated the "spaghetti" diagrams for the 60-km ensemble means only (to maintain legibility we did not include additional lines into Figs. 6 and 7). Note that the spaghetti diagrams for the 60-km ensemble means are quite close to those of the full ensemble means shown in Figs. 6 and 7. However, the 60-km ensemble members have a larger dispersion for both seasons than those of 100 km. This result suggests that larger ensembles are needed when using higher resolution.

Figures 6 and 7 were reproduced for 2, 4, . . . , 10 yr (not shown) to analyze the time evolution of the spaghetti pattern. The basic patterns have already been formed after 2 yr but the secondary pattern features continue to evolve after that. For 500-hPa heights, the DJF patterns converge after 4 yr. The JJA patterns converge more slowly, after 6–8 yr, although in all cases

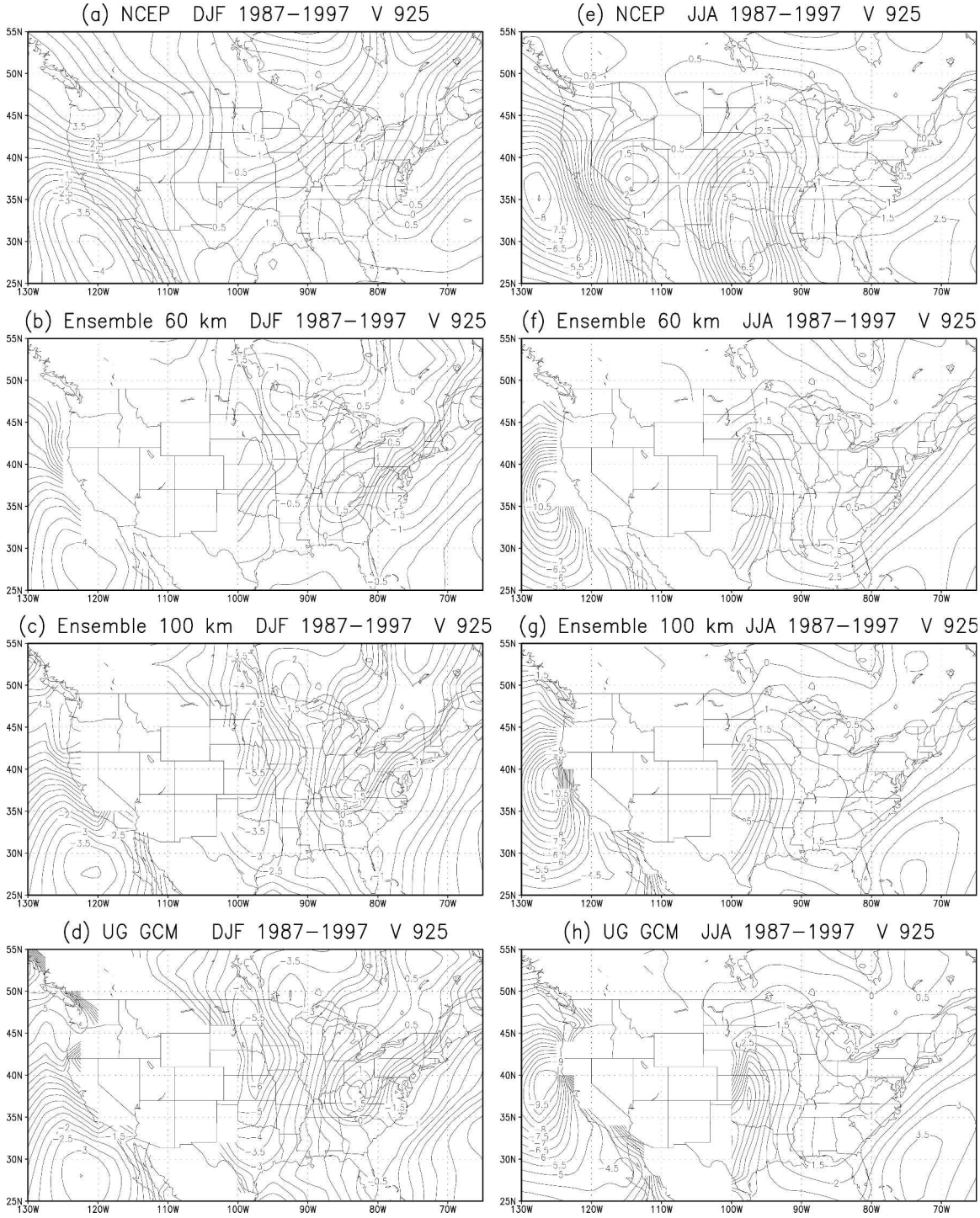

FIG. 5. The 11-yr (1987–97) 925-hPa meridional wind component for (left) DJF and (right) JJA for the (a), (e) NCEP–NCAR global reanalyses, (b), (f) the 60-km ensemble, (c), (g) the 100-km ensemble, and (d), (h) UG-GCM. The contour interval is 1 m s^{-1}.

the differences were minor. For the 500-hPa meridional winds, both the DJF and JJA patterns mostly converge by 4 yr although some secondary pattern features continue to evolve during 6–8 yr. Therefore, the spaghetti contour structures practically converge toward stable patterns mostly after 4 yr with some minor changes occurring during the next 2–4 yr so that the complete pattern convergence takes approximately 6–8 yr.

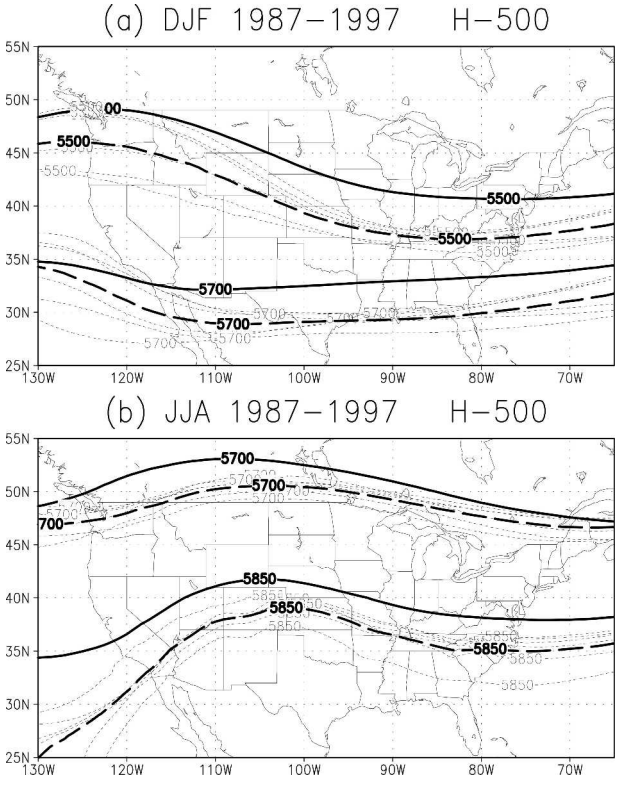

FIG. 6. Selected contours of 500-hPa heights for the individual members of the ensemble (thin dashed lines), their mean (thick dashed line), and the NCEP–NCAR reanalysis (thick solid line): (a) DJF (contours: 5500 and 5700 m) and (b) JJA (contours: 5700 and 5850 m).

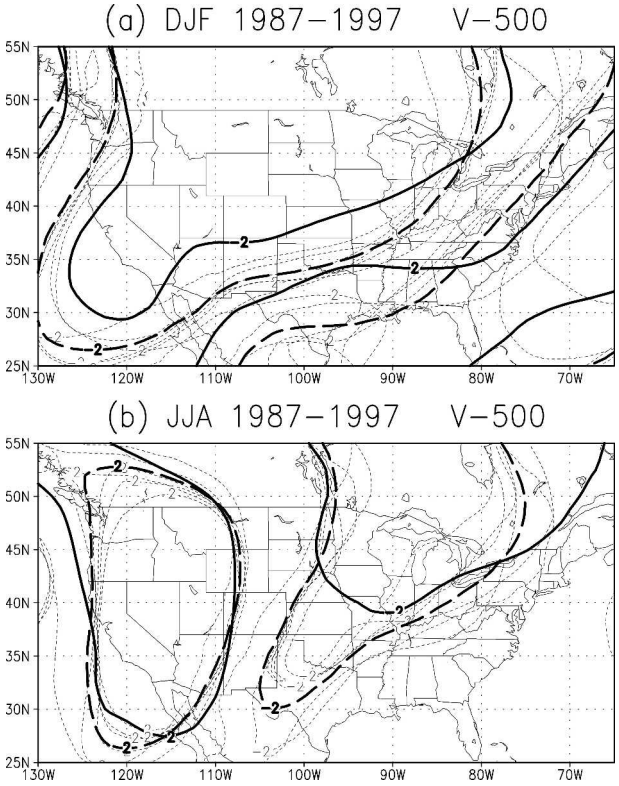

FIG. 7. As in Fig. 6, but for the 500-hPa meridional wind. Selected contours are -2 and 2 m s^{-1} for both seasons.

4. Simulated precipitation

The mean and interannual variability of the simulated precipitation patterns are presented for the 10-yr period, 1987–1996, in order to use for verification the University of Delaware dataset, which ends in December 1996. The results of a single experiment with the basic GEOS UG-GCM are included as a reference point. The mesoscale features are partly smoothed by ensemble and time averaging. However, the individual ensemble members (not shown for brevity) contain more mesoscale features that contribute to the ensemble mean.

a. Multiyear ensemble mean

The 10-yr mean precipitation patterns for observations and model simulations are shown in Fig. 8. The two observation-based datasets (Figs. 8a,b) resemble each other, apart from the mesoscale features captured only in the University of Delaware precipitation dataset. The most noticeable mesoscale features are found in the northwestern United States, where the University of Delaware precipitation field has two maxima (associated with the Cascades and the Rockies) as opposed to the CMAP field that shows one broad area.

The ensemble means (60 km, 100 km, and combined shown in Figs. 8c–e) are in agreement with the observed patterns over the Midwest and eastern United States, and more clearly on the elongated maximum over the Atlantic Ocean and the maximum over the northwestern United States. In the last case, the ensemble simulations capture the double pattern, although its area seems to be broader. The northwestern U.S. region is one of the most complex regions to get accurate observed and model estimates of precipitation; see Luo et al. (2005) for a discussion on the precipitation estimates over the region, and their impact on the surface water budgets.

At finer regional scales, the University of Delaware data show large precipitation along the northern coast of the Gulf of Mexico and over Tennessee and other small centers over the Appalachians. These mesoscale features seem to be related to the Appalachian Mountains and the east coast land–sea differences. The area is, in our view, of an interest for testing mesoscale models, especially for mesoscale climate studies in general

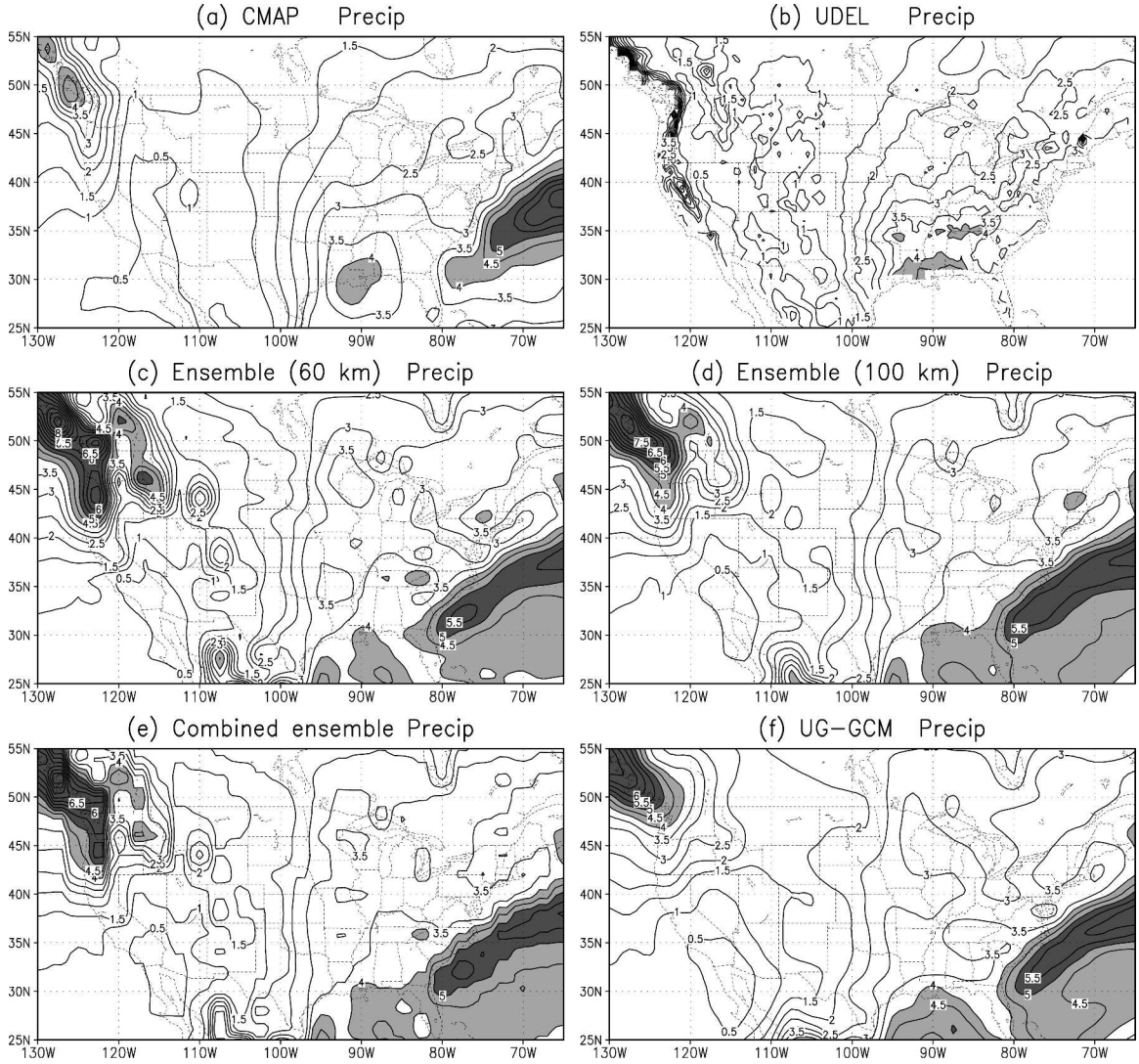

FIG. 8. The 10-yr (1987–96) mean precipitation for (a) CMAP, (b) the University of Delaware rain gauge data, (c) 60-km ensemble mean, (d) 100-km ensemble mean, (e) the combined ensemble, and (f) the uniform GCM simulation. The contour interval is 0.5 mm day^{-1}. The areas with precipitation above 4 mm day^{-1} are shaded.

and for the subregion in particular. The 60-km SG-GCM ensemble simulations (Fig. 8c) show features that resemble the University of Delaware data patterns over the subregion. The coarser-resolution 100-km ensemble mean (Fig. 8d) and the basic UG-GCM (Fig. 8f) show quite similar basic regional precipitation patterns but fail to produce all the aforementioned features of the mesoscale precipitation pattern over the southeastern United States. Finally, despite these being annual means, the pattern of the North American monsoon over western Mexico (Fig. 8b) can be noticed, particularly in the SG-GCM simulations (Figs. 8c–e).

To further substantiate that the improvements are the result of the better-resolved dynamics and boundary forcing, we show mesoscale features in large-scale (P_{LS}) and convective precipitation (P_{CON}) as well as in the ratio of P_{CON} to total precipitation (P_{TOT}), for 60-km ensemble integrations versus that of UG-GCM (Fig. 9). The 60-km ensemble means (Figs. 9a,c,e) contain the following mesoscale features that are not as evident in the UG-GCM simulation (Figs. 9b,d,f): P_{LS}, P_{CON}, and the ratio P_{CON}/P_{TOT} for the 60-km ensemble mean show larger values and sharper patterns compared to those of UG-GCM (Figs. 9b,d,f) over the Appalachian and Rocky Mountains. Also, P_{LS} is stronger over the Great Lakes area (Figs. 9a,b).

Convective precipitation P_{CON} and especially P_{LS} show increased values and sharper patterns over the

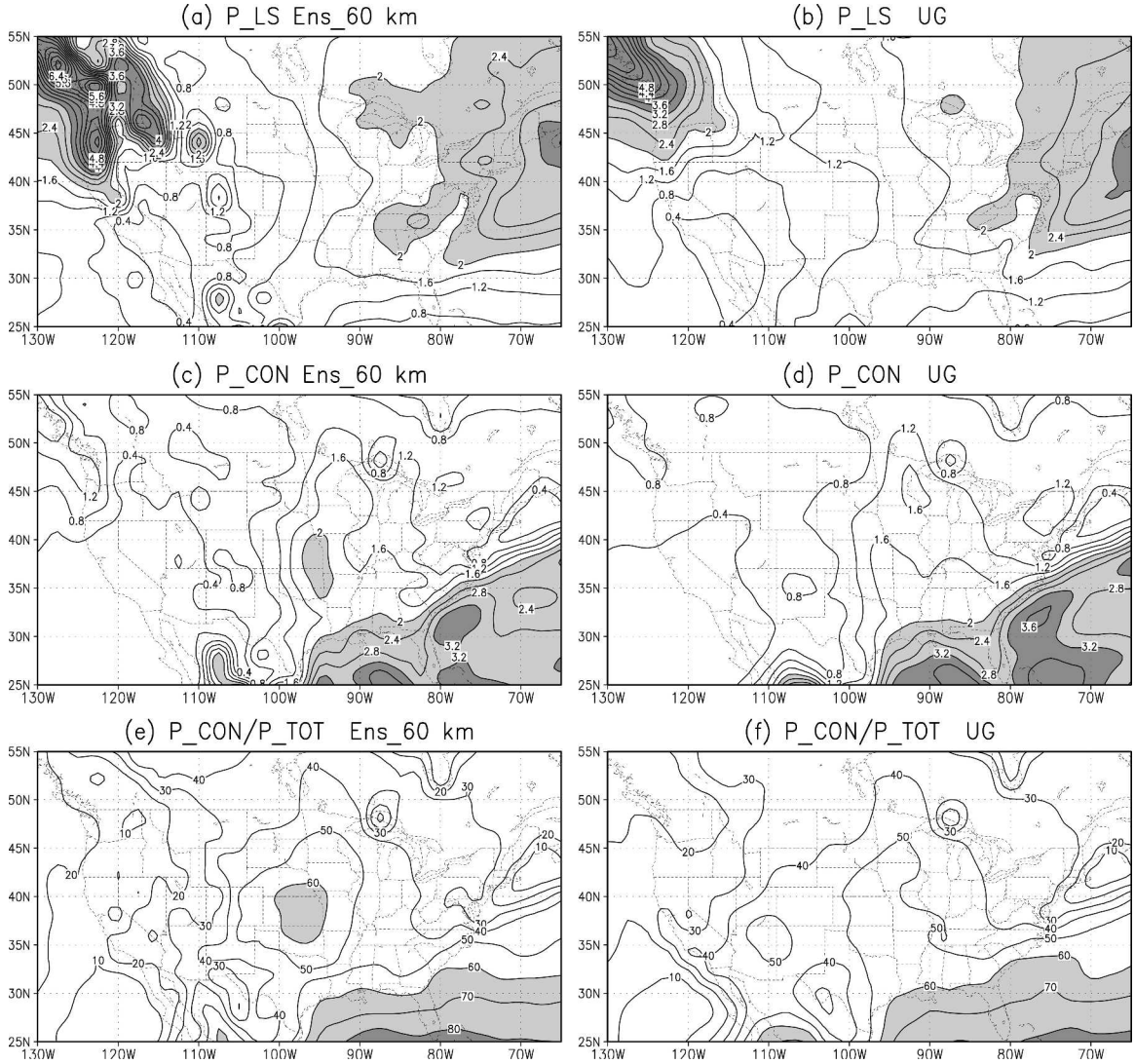

FIG. 9. The 11-yr (1987–97) mean precipitation for (left) 60-km ensemble mean and (right) UG-GCM for (a), (b) large-scale precipitation, (c), (d) convective precipitation, and (e), (f) the ratio of convective to total precipitation. The contour interval is 0.4 mm day^{-1} for (a)–(d) and 10% for (e) and (f).

northwestern United States, Canadian British Columbia, and the surrounding ocean associated with the North Pacific storm track, and over central-western Mexico associated with the North American monsoon (Figs. 9a,c and 9b,d, respectively). Convective precipitation P_{CON} and the ratio $P_{\mathrm{CON}}/P_{\mathrm{TOT}}$ have a more pronounced south–north structure and the maxima over the Midwest (Figs. 9c,e and 9d,f, respectively). It is noteworthy that the ratio for the 60-km ensemble is consistent in magnitude and pattern with that of the UG-GCM (Figs. 9e,f), but with new mesoscale features as indicated above.

We also calculated global and regional area means for precipitation. The area means P_{LS} and P_{CON} (and P_{TOT}) are close in magnitude for global and regional domains, correspondingly for both ensemble and UG-GCM integrations. More specifically, the global ratio of P_{LS} to P_{TOT} is 35% and 40% for the ensemble and UG-GCM integrations, respectively, but it is larger (55% and 60%, respectively) over the region. It indicates the relative increase of P_{LS} over the better-resolved area of interest. The 100-km and combined six-member ensemble area means are quite similar to those of the 60-km ensemble indicated above. It is seen that global precipitation is dominated by tropical convection whereas for our region located in the extratropics P_{LS} is larger than in the Tropics.

For the further discussion on downscaling provided

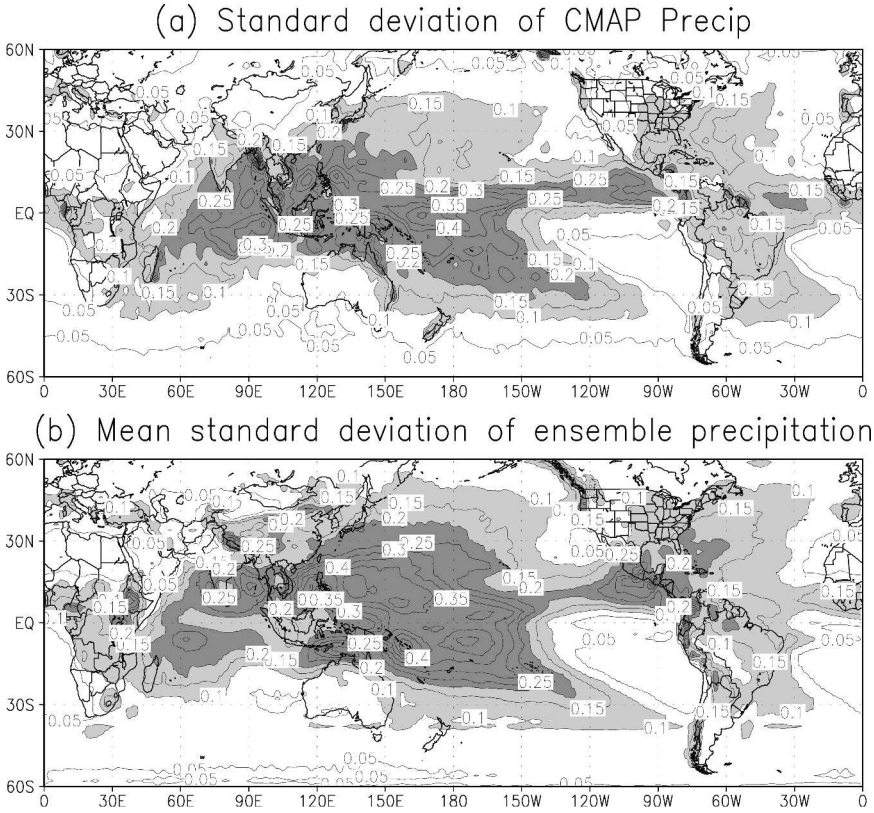

FIG. 10. Near-global (60°S to 60°N) standard deviation distribution of (a) CMAP precipitation and (b) ensemble mean precipitation. The annual cycle has been removed. The contour interval is 0.04 mm day^{-1}, and the values larger than 0.12 mm day^{-1} are shaded.

by using fine regional resolution within a stretched grid for model dynamics while using coarser resolution for model physics, we produced spherical harmonic spectra for large-scale, convective, and total precipitation for the 11-yr 60-km ensemble and UG-GCM simulations, aimed at comparing them for the meso- and adjacent scales. The spectra are calculated for monthly means and then averaged for the 11-yr period. Although these are the global spectra they reflect generating mesoscales due to stretching. For large and medium scales, with wavenumbers 1–40, the 60-km ensemble and UG-GCM spectra are quite close to each other. They would be even closer if 6-hourly, not monthly, means were used for the spectra calculations as was shown by Fox-Rabinovitz et al. (2002). However, for the wavenumbers 41–90, the spectral range that represents the smaller scales or meso- and adjacent scales, the impact is quite significant in terms of producing smaller scales through stretching. Namely, the increase for the 60-km ensemble mean spectral amplitudes for the smaller meso- and adjacent scale range versus those of the UG-GCM simulation is 29% and 51% for convective and large-scale precipitation, respectively. The similar increase for total precipitation is 45%. Therefore, the major impact on smaller, meso- and adjacent scales from stretching is obtained for large-scale precipitation. It is noteworthy that we did not observe any noise or systematic errors generated at meso- and larger scales, especially for time- or area-averaged fields, when analyzing the SG-GCM simulations for this and previous relevant studies.

The results presented in this and the previous sections show a measurable impact in terms of downscaling provided through stretching or producing more realistic mesoscale features by the SG-GCM ensemble as compared to those of the UG-GCM simulation.

b. Ensemble dispersion

Figure 10 shows (in addition to the regional patterns shown below) the standard deviation for a large part of the globe, 60°S to 60°N (the polar domains are not shown because of a lack of observational data there), for CMAP and six-member ensemble mean precipitation. The mean annual cycle has been subtracted before producing the standard deviation distributions here and for the regional distributions shown below as well. The

near-global standard deviation pattern for ensemble mean precipitation is quite similar to that of CMAP (Figs. 10a,b). Standard deviations are larger in the tropical domain. Outside the Tropics, we also see larger standard deviations over the eastern United States and the surrounding Atlantic Ocean. Note that larger standard deviations appear in other parts of the extratropics with relatively fine resolution (in one direction only) due to longitudinal stretching (such as southern South America and the surrounding Atlantic Ocean), or latitudinal stretching (such as northern China, Japan, and the large adjacent part of the northern Pacific Ocean). Also, larger standard deviations are shown in the extratropical southern Pacific Ocean although variable resolution is coarser there.

Figure 11 presents the regional 10-yr precipitation standard deviation for the observations (CMAP and University of Delaware) and for the ensemble (the standard deviation was averaged for all the ensemble members). The areas with increased standard deviation (dark shaded) for the observed precipitation (Figs. 11a,b) are located in the southeastern United States and south-central Midwest, and in the northwestern United States/southwestern Canada. In addition, the University of Delaware dataset at finer resolution shows the increased values along the Appalachians.

Basically, the same pattern of precipitation standard deviation is obtained for the ensemble simulation (Fig. 11c). Even the magnitudes over the eastern half of the United States including the Appalachians are close to the University of Delaware estimates. The northwestern maxima extend toward central and southern California consistently with observations (Figs. 11a,b). The secondary maximum over Idaho is shown in both the ensemble (Fig. 11c) and the University of Delaware (Fig. 11b) patterns, although the latter is weaker. Another secondary maximum over western Mexico is much stronger in the ensemble field (Fig. 11c). It is possible that the model may be overestimating the magnitude (either in intensity or seasonal duration) of the monsoon.

The standard deviation pattern in the Atlantic Ocean off the U.S. east coast is similar for CMAP and the ensemble mean (Figs. 11a,c), although the values are smaller for CMAP than for the ensemble mean. Over the rest of the region, namely over the western United States, northeastern United States, northern Midwest, and the Pacific Ocean off the coast of southern California and Baja peninsula, the variances are similar but larger in the ensemble than in CMAP.

Note that over the eastern United States (east of 100°W) and especially over the southeastern United States and Midwest where both precipitation and its variances are larger than over the rest of the region, the variance differences between CMAP and ensemble mean are quite limited, mostly within 10% and not exceeding 20%. Over the areas with smaller precipitation and its variances, mostly over the western United States, the differences are also small. It confirms that the variance patterns show a significant overall similarity for the entire region.

A typical measure of the ensemble spread (e.g., Hacker and Baumhefner 2004) is given by the equation

$$\sigma^2 = \frac{1}{N}\sum_{i=1}^{N} \langle [P(s,t) - Q(s,t) - \langle P(s,t) - Q(s,t)\rangle]^2\rangle,$$

where N is the number of possible pairs of simulations in the ensemble; P, Q are individual simulations; (s, t) are space and time; and the operator $<>$ is a spatial average (in our case) over the region delimited by 25°–50°N, 125°–75°W. Figure 12 presents the mean annual cycle of the square root of the ensemble spread. In the precipitation time series (not shown), there is large interannual variability with some peaks over 4 mm day^{-1}. On the average, the values are largest during winter and spring, and then decay during summer and early fall with a minimum of less than 1 mm day^{-1} (Fig. 12).

c. Signal-to-noise ratio

Let us consider the noise, signal, and signal-to-noise (STN) ratio for the 11-yr (1987–97) SG-GCM six-member ensemble mean precipitation presented in Fig. 13 for a near-global domain and in Fig. 14 for the region of interest. The signal is measured by the interannual variance of the ensemble mean about the ensemble climate mean, and the noise is measured by the variance of the individual ensemble members about each year's ensemble mean (e.g., Chang et al. 2000). Namely, signal $s^2 = n/(n-1)\{(x^* - [x^*])^2\}$, noise $n^2 = m/(m-1)\{(x - x^*)^2\}^*$, and STN ratio $R = s^2/n^2$, where * denotes a mean over $m = 6$ ensemble members, and [] denotes a mean over $n = 11$ yr.

The near-global distributions of noise and signal (Figs. 13a,b) have quite similar patterns, with larger values in the Tropics and over the extratropics in the Pacific and Indian Oceans. Noise is predominantly larger than signal (notice different contour intervals for Figs. 13a,b). Also, noise is strong in the southern ocean storm tracks, between 40° and 55°S. The STN ratios $R \geq 1.5$ are also shown mostly in the Tropics (Fig. 13c). In the extratropics, the STN ratios $R \geq 1.5$ appear over the area of interest and extend to Canada where resolution is still quite fine due to stretching. These results suggest a possibly better predictability of the SG-GCM en-

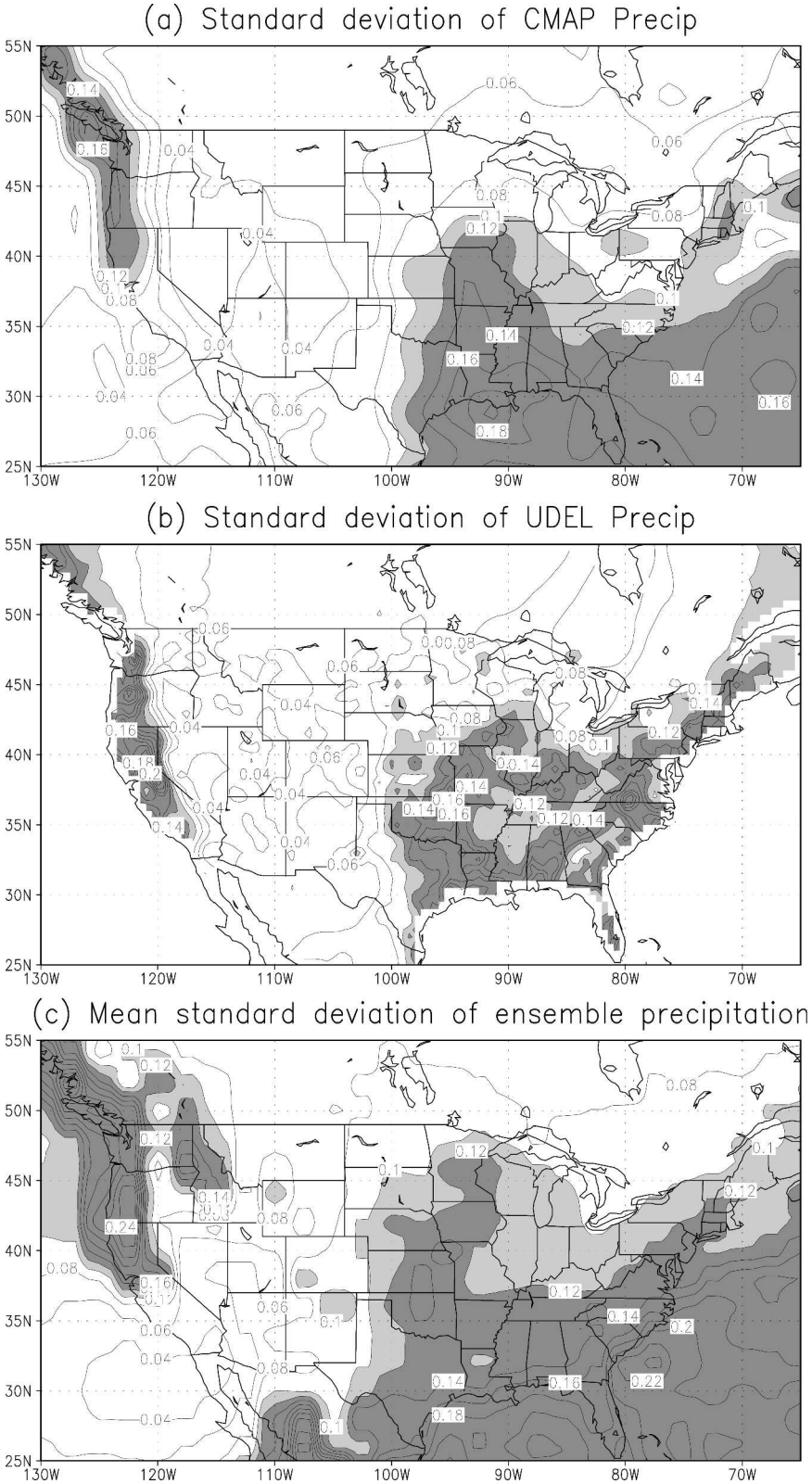

FIG. 11. Regional standard deviation of (a) CMAP precipitation, (b) University of Delaware precipitation, and (c) the ensemble mean precipitation. The annual cycle has been removed. Contour interval is 0.02 mm day^{-1}, and values larger than 0.1 mm day^{-1} are shaded.

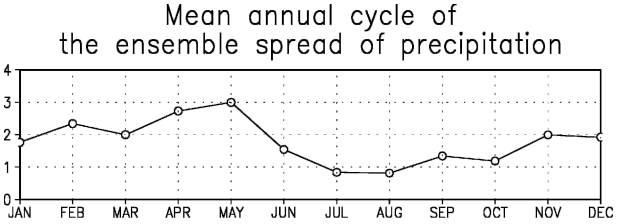

FIG. 12. Mean annual cycle of the square root of the ensemble spread of precipitation. Units are mm day^{-1}.

semble for the area of interest located outside the Tropics.

The choice of $R \geq 1.5$ is explained next. We can use the following relationship between an STN ratio and a correlation coefficient r: STN $= r\sqrt{m}/\sqrt{(1 + r^2)}$, where $m = 6$ is the number of ensemble members. For reaching the predictability level of $r = 0.7$ we need STN ratios $R > 1.4$. Chang et al. (2000) point out that STN is inflated for small/limited ensembles. It means that STN > 1.5 will approximately correspond to $r \geq 0.6$. This is an approximate estimate used here just for the justification of using $R \geq 1.5$ for our discussion and for the corresponding shading used for STN ratios in Figs. 13c and 14c.

Let us consider now the regional distributions of noise, signal, and STN ratios presented in Fig. 14. The most relevant aspect noticed in Fig. 14c is that significant ratios $R \geq 1.5$ are obtained over a substantial part of the United States, namely over the Midwest and the adjacent Rocky Mountains and south-central Canada as well as over northern Mexico and southern Texas. A strong center, with the ratio R up to 7, is shown at the center of the region over the central Midwest. Note that the ratios $R \geq 1.5$ imply that the signal (Fig. 14b) prevails over the noise (Fig. 14a), and we show the area by shading in Fig. 14c. The ratios $R < 1.5$ are obtained for the east and west coast areas and for the southeastern United States (Fig. 14c). It is likely that the ratios for the coastal areas with a strong impact from the land–sea difference forcing can be reduced when using larger ensembles for finer resolutions.

To test that the signal is significantly larger than the noise (or that the signal-to-noise ratio is significantly greater than one), we included a test for the statistical significance of the signal for F distribution assuming normal distribution for random variables and $[n - 1, n(m - 1)]$ degrees of freedom. In our case, with $n = 11$, $m = 6$ specified above, and therefore with (10, 55) degrees of freedom, the 5% of the statistical significance for the signal is obtained for $F_{10,55}(0.05) = 2.01$, which is equivalent to the STN $= 0.33$. The latter number is relatively large because of our limited ensemble size. However, we used quite larger STN ratios like $R \geq 1.5$ for our analysis.

Larger ensembles may help to depict more accurately the features associated with rather sharp land–sea differences, but it is also possible that the regions are largely unpredictable, regardless of the number of members in the ensemble or the length of the integration. The STN ratios close to $R \sim 1.5$ are obtained over the Appalachians and are even larger over the Rockies (Fig. 14c). In this case, it is possible that the appropriately simulated orographic effects are contributing to the relatively large STN ratios. The regional noise and signal are basically consistent with those of obtained for the basic UG-GCM reported by Schubert et al. (2001) and Chang et al. (2000), and for other GCMs (Shukla et al. 2000), and indicate the reasonable predictability skill for the SG-GCM ensemble integrations.

5. Conclusions

A set of 11-yr (1987–97) simulations have been performed with the stretched-grid version of the GEOS GCM with enhanced resolution over the United States. Limited ensembles, three members with 60- and other three members with 100-km regional resolution, for a total of six ensemble members, have been produced. In both cases, the model physics is resolved on an intermediate uniform latitude–longitude grid of $2° \times 2.5°$. For comparison purposes, an additional simulation has been performed using a global uniform $2° \times 2.5°$ grid with the same number of global grid points as those of the above stretched grids. The simulations of prognostic fields were compared to the NCEP–NCAR reanalyses, while precipitation fields were compared to high-resolution—$0.5° \times 0.5°$—gauge precipitation dataset (land only) produced by the University of Delaware. CMAP estimates of precipitation were employed to supplement the gauge-only dataset, in particular over the oceans. The simulated ensemble means are discussed in terms of their ability to reproduce regional patterns, especially their mesoscale features. The main results are summarized as follows:

1) The ensemble simulations have a reasonable representation of the global-to-regional-scale patterns, although over the United States there tends to be a negative bias in height and meridional wind during winter. While the bias is also present during summer, it is of a much smaller magnitude than in winter.
2) The multiyear ensemble mean low-level winds at 60-km resolution compare well with those of the NCEP–NCAR reanalysis in terms of reproducing

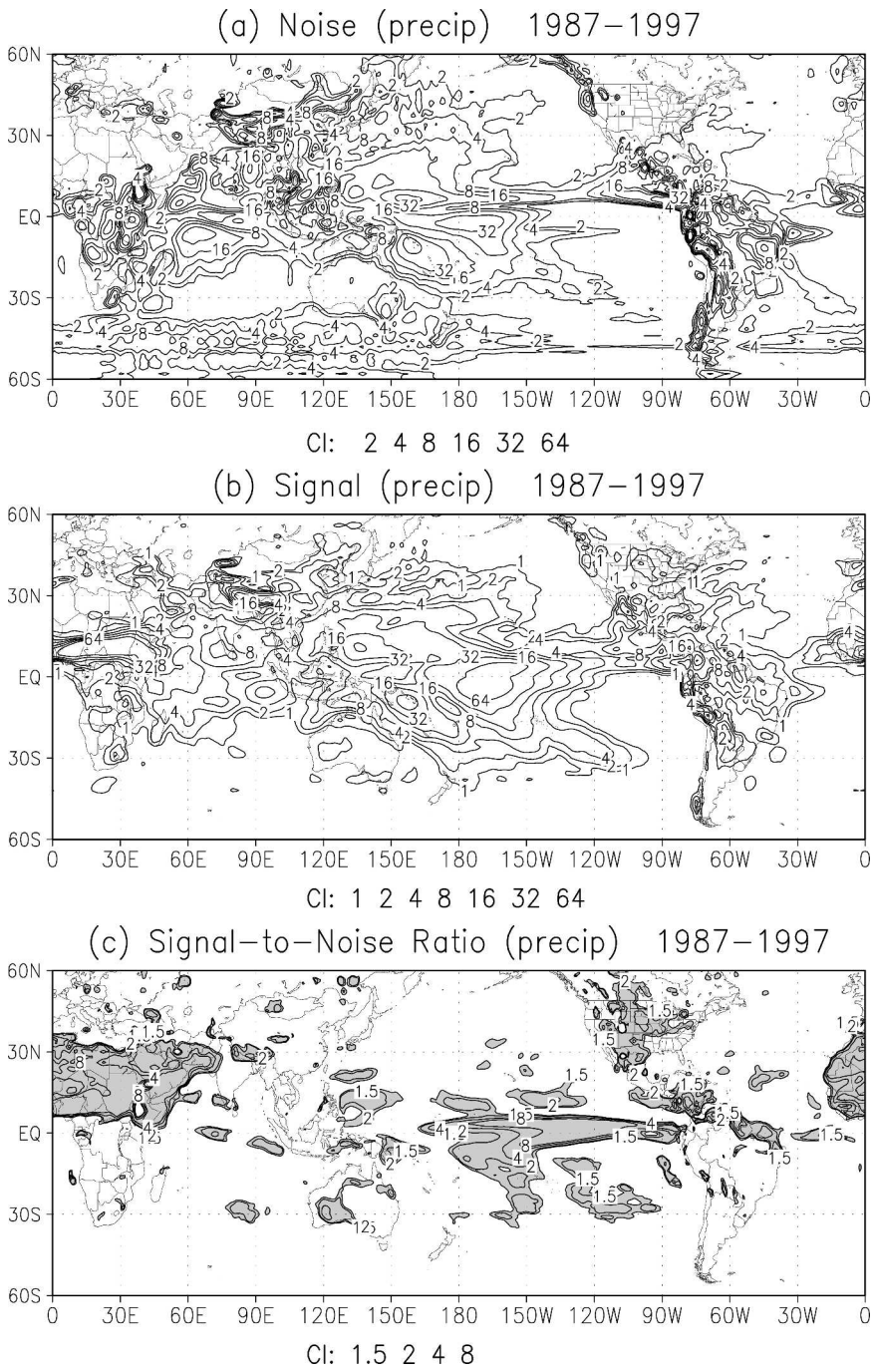

FIG. 13. Near-global (60°S to 60°N) distribution of (a) noise, (b) signal, and (c) STN ratio for 11-yr (1987–97) six-member ensemble mean precipitation. The contour intervals in mm day^{-1} for (a) and (b), and dimensionless for (c), are depicted below each panel. The areas with the STN ratios larger than 1 are shaded for (c).

regional and subregional mesoscale pattern features. Coarser resolutions (100-km ensemble and UG) tend to have a stronger southward wind east of the Rockies during winter that is not supported by the observations.

3) The multiyear ensemble mean precipitation for 60-km resolution appear to be closer overall than that of 100-km, and especially UG-GCM to high-resolution observations (the University of Delaware dataset) and to CMAP.

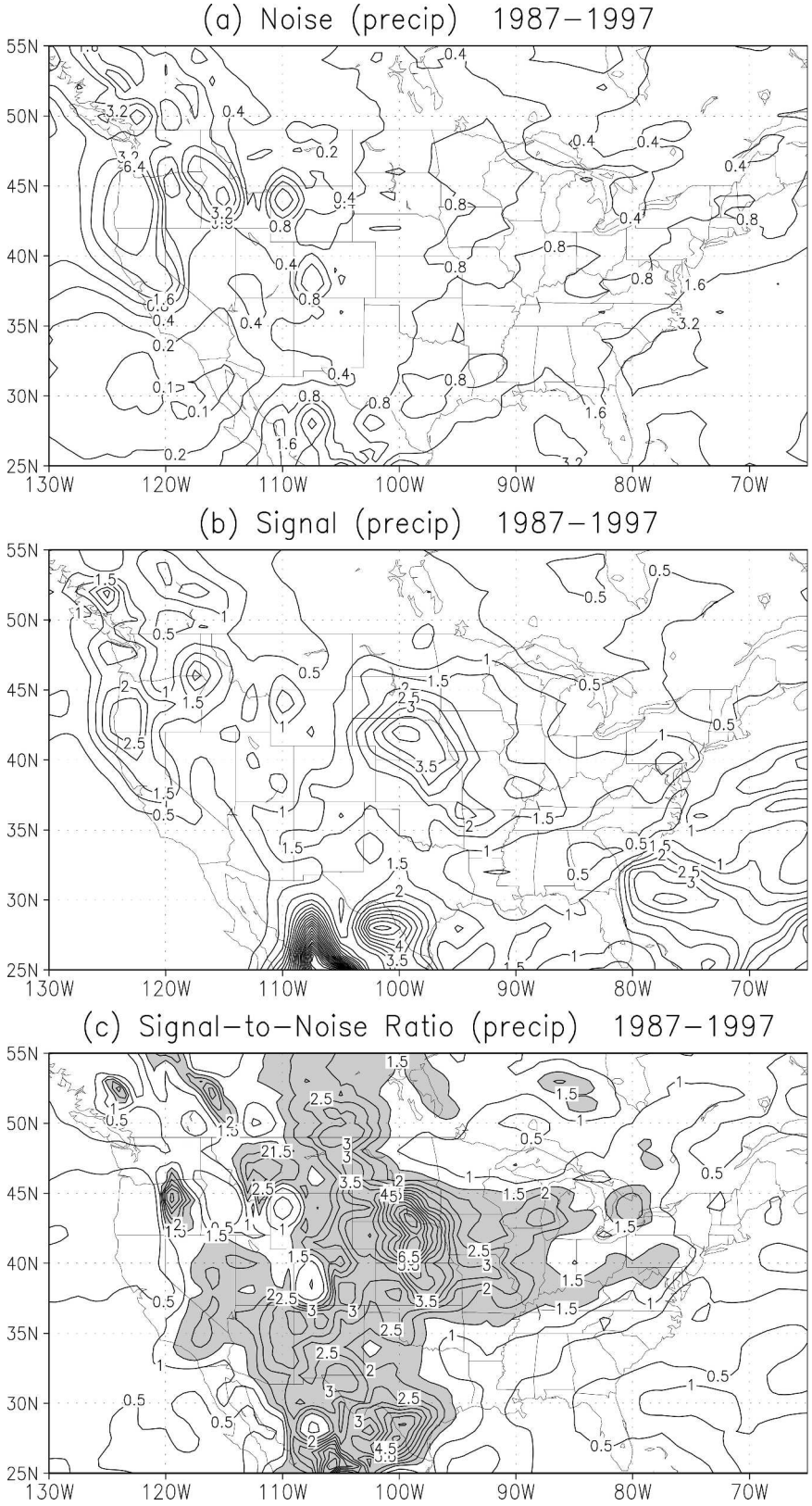

FIG. 14. (a) Regional noise, (b) signal, and (c) STN ratio for 11-yr (1987–97) six-member ensemble mean precipitation. For (a), the variable/exponential contour intervals 0.1, 0.2, 0.4, 0.8, . . . , 6.4 mm day^{-1} are used; for (b) and (c) the contour interval is 0.5 mm day^{-1}. The areas shaded in (c) are where the STN ratios are larger than 1.5.

4) The precipitation variance patterns for the ensemble mean are in good agreement with those of observations.
5) The signal-to-noise ratio *R* for 11-yr ensemble precipitation shows that signal is prevailing over noise over a significant part of the region of interest, especially over its central part, the Midwest. For the narrow coastal areas the ratios are smaller and larger ensembles and finer regional resolution may be needed to account for sharp land–sea differences.

The results of the study show that even using limited ensemble integrations with a state-of-the-art stretched-grid GCM is beneficial for reducing the uncertainty of the multiyear regional climate simulation, especially when using finer 60-km regional resolution.

Acknowledgments. The careful comments of three anonymous reviewers are greatly appreciated, as they helped to improve this paper. This study is based upon work supported by the National Science Foundation under Grant 0105839, the Department of Energy Grant ER63197-0007185, and NASA Grant NAG511577.

REFERENCES

Allen, D. J., K. E. Pickering, and M. Fox-Rabinovitz, 2004: Evaluation of pollutant outflow and CO sources during TRACE-P using model-calculated, aircraft-based, and MOPITT-derived CO concentrations. *J. Geophys. Res.,* **109,** D15S03, doi:10.1029/2003JD004250.

Arakawa, A., and V. R. Lamb, 1981: A potential enstrophy and energy conserving scheme for the shallow water equations. *Mon. Wea. Rev.,* **109,** 18–36.

——, and M. J. Suarez, 1983: Vertical differencing of the primitive equations in sigma coordinates. *Mon. Wea. Rev.,* **111,** 34–45.

Berbery, E. H., and M. S. Fox-Rabinovitz, 2003: Multiscale diagnosis of the North American monsoon system with a variable resolution GCM. *J. Climate,* **16,** 1929–1947.

Brown, J. A., and K. Campana, 1978: An economical time differencing scheme for numerical weather prediction. *Mon. Wea. Rev.,* **106,** 1125–1136.

Chang, Y., S. D. Schubert, and M. J. Suarez, 2000: Boreal winter predictions with the GEOS-2 GCM: The role of boundary forcing and initial conditions. *Quart. J. Roy. Meteor. Soc.,* **126,** 2293–2321.

Chou, M.-D., and M. J. Suarez, 1994: An efficient thermal infrared radiation parameterization for use in GCMs. NASA Tech. Memo. 104606, Vol. 3, 85 pp. [Available from NASA GSFC Data Assimilation Office, Greenbelt, MD 20771.]

Cote, J., 1997: Variable resolution techniques for weather prediction. *Meteor. Atmos. Phys.,* **63,** 31–38.

——, M. Roch, A. Staniforth, and L. Fillion, 1993: A variable-resolution semi-Lagrangian finite-element global model of the shallow-water equations. *Mon. Wea. Rev.,* **121,** 231–243.

——, S. Gravel, A. Metot, A. Patoine, M. Roch, and A. Staniforth, 1998: The operational CMC/MRB Global Environmental Multiscale (GEM) model. Part I: Design considerations and formulation. *Mon. Wea. Rev.,* **126,** 1373–1395.

Deque, M., and J. P. Piedelievre, 1995: High resolution climate simulation over Europe. *Climate Dyn.,* **11,** 321–339.

——, P. Marquet, and R. Jones, 1998: Simulation of climate change over Europe using a global variable resolution general circulation model. *Climate Dyn.,* **14,** 173–189.

Fox-Rabinovitz, M. S., 1974: Economical explicit and semi-implicit integration schemes for forecast equations. *Sov. Meteor. Hydrol.,* **11,** 11–19.

——, 1988: Dispersion properties of some regular and irregular grids used in atmospheric models. *Proc. Eighth Conf. on Numerical Weather Prediction,* Baltimore, MD, Amer. Meteor. Soc., 784–789.

——, 2000: Regional climate simulation of the anomalous U.S. summer events using a variable-resolution stretched-grid GCM. *J. Geophys. Res.,* **105** (D24), 29 635–29 646.

——, G. L. Stenchikov, M. J. Suarez, and L. L. Takacs, 1997: A finite-difference GCM dynamical core with a variable-resolution stretched grid. *Mon. Wea. Rev.,* **125,** 2943–2968.

——, ——, ——, ——, and R. C. Govindaraju, 2000: An uniform and variable resolution stretched-grid GCM dynamical core with real orography. *Mon. Wea. Rev.,* **128,** 1883–1898.

——, L. L. Takacs, and M. J. Suarez, 2001: A variable resolution stretched grid GCM: Regional climate simulation. *Mon. Wea. Rev.,* **129,** 453–469.

——, ——, and R. C. Govindaraju, 2002: A variable-resolution stretched-grid general circulation model and data assimilation system with multiple areas of interest: Studying the anomalous regional climate events of 1998. *J. Geophys. Res.,* **107,** 4768, doi:10.1029/2002JD002177.

Hacker, J., and D. Baumhefner, 2004: Flow-dependent calibration of ensemble spread using forecast spectra. Preprints, *20th Conf. on Weather Analysis and Forecasting,* Seattle, WA, Amer. Meteor. Soc., CD-ROM, 23.5.

Helfand, H. M., and J. C. Labraga, 1988: Design of a non-singular level 2.5 second-order closure model for the prediction of atmospheric turbulence. *J. Atmos. Sci.,* **45,** 113–132.

——, M. Fox-Rabinovitz, L. Takacs, and A. Molod, 1991: Simulation of the planetary boundary layer and turbulence in the GLA GCM. *Proc. Ninth Conf. on Numerical Weather Prediction,* Denver, CO, Amer. Meteor. Soc., 514–517.

Kalnay, E., and Coauthors, 1996: The NCEP/NCAR 40-Year Reanalysis Project. *Bull. Amer. Meteor. Soc.,* **77,** 437–471.

Lander, J., and B. J. Hoskins, 1997: Believable scales and parameterizations in a spectral model. *Mon. Wea. Rev.,* **125,** 292–303.

Lorenz, E. N., 1960: Energy and numerical weather prediction. *Tellus,* **12,** 364–373.

Luo, Y., E. H. Berbery, and K. E. Mitchell, 2005: The operational Eta Model precipitation and surface hydrologic cycle of the Columbia and Colorado basins. *J. Hydrometeor.,* **6,** 341–370.

McGregor, J. L., 1997: Regional climate modeling. *Meteor. Atmos. Phys,* **63,** 105–117.

——, and M. R. Dix, 2001: The CSIRO conformal-cubic atmospheric GCM. *UTAM Symposium on Advances in Mathematical Modelling of Atmosphere and Ocean Dynamics,* P. F. Hodnett, Ed., Kluwer, 197–202.

Moorthi, S., and M. J. Suarez, 1992: Relaxed Arakawa Schubert: A parameterization of moist convection for general circulation models. *Mon. Wea. Rev.,* **120,** 978–1001.

Park, R. J., K. E. Pickering, D. J. Allen, G. L. Stenchikov, and M. S. Fox-Rabinovitz, 2004: Global simulation of tropospheric ozone using the University of Maryland Chemical Transport Model (UMD-CTM). 2. Regional transport and

chemistry over the central United States using a stretched grid. *J. Geophys. Res.,* **109,** D09303, doi:10.1029/2003JD004269.

Sadourny, R., 1975: The dynamics of finite difference models of the shallow water equations. *J. Atmos. Sci.,* **32,** 680–689.

Schubert, S., M. J. Suarez, and Y. Chang, 2001: The impact of ENSO on extra-tropical low-frequency noise in seasonal forecasting. *J. Climate,* **14,** 2351–2365.

Schuman, F. G., 1971: Resuscitation of an integration procedure. NMC Office Note 54, 55 pp. [Available from NCEP/NOAA, 5200 Auth Road, Camp Springs, MD 20746.]

Shapiro, R., 1970: Smoothing, filtering and boundary effects. *Rev. Geophys. Space Phys.,* **8,** 359–387.

Shukla, J., and Coauthors, 2000: Dynamical seasonal prediction. *Bull. Amer. Meteor. Soc.,* **81,** 2593–2606.

Suarez, M. J., and L. L. Takacs, 1995: Documentation of the Aries/GEOS Dynamical Core Version 2. NASA Tech. Memo. 104606, NASA Goddard Space Flight Center, Greenbelt, MD, 103 pp. [Available from Data Assimilation Office, NASA GSFC, Greenbelt, MD 20771.]

Sud, Y. C., and A. Molod, 1988: The roles of dry convection, cloud-radiation feedback processes and the influence of recent improvements in the parameterization of convection in the GLA GCM. *Mon. Wea. Rev.,* **116,** 2366–2387.

Takacs, L. L., M. J. Suarez, W. Sawyer, and M. S. Fox-Rabinovitz, 1999: Filtering techniques on a stretched grid GCM. NASA Tech. Memo. 104606, Vol. 15, 29 pp. [Available from Data Assimilation Office, NASA GSFC, Greenbelt, MD 20771.]

Takle, E. S., and Coauthors, 1999: Project to Intercompare Regional Climate Simulations (PIRCS): Description and initial results. *J. Geophys. Res.,* **104** (D16), 19 443–19 461.

Vichnevetsky, R., 1987: Wave propagation and reflection in irregular grids for hyperbolic equations. *Appl. Numer. Math.,* **2,** 133–166.

Willmott, C. J., and K. Matsuura, cited 2001: Terrestrial air temperature and precipitation: Monthly and annual time series (1950–1999) (Version 1.02). Center for Climatic Research, University of Delaware, Newark, DE. [Available online at http://climate.geog.udel.edu/~climate/.]

Xie, P., and P. A. Arkin, 1997: Global precipitation: A 17-year monthly analysis based on gauge observations, satellite estimates and numerical model outputs. *Bull. Amer. Meteor. Soc.,* **78,** 2539–2558.

Zhou, J., Y. C. Sud, and K.-M. Lau, 1996: Impact of orographically induced gravity wave drag in the GLA GCM. *Quart. J. Roy. Meteor. Soc.,* **122,** 903–927.